International Journal of Greenhouse Gas Control 99 (2020) 103075

Contents lists available at ScienceDirect

International Journal of Greenhouse Gas Control

journal homepage: www.elsevier.com/locate/ijggc

Continuum scale modelling of salt precipitation in the context of CO_2 storage in saline aquifers with MRST compositional

S. Parvin[a], M. Masoudi[b], A. Sundal[b], R. Miri[b,c,*]

[a] Ahwaz Faculty of Petroleum, Petroleum University of Technology, Ahwaz, Iran
[b] Department of Geosciences, University of Oslo, PO. Box 1047 Blindern, N-0316 Oslo, Norway
[c] School of Chemical Engineering, Iran University of Science and Technology (IUST), P.O. Box 16765-163, Tehran, Iran

ARTICLE INFO

Keywords:
Salt precipitation
Self-enhancing
Injectivity
CCS
CO_2 storage

ABSTRACT

Carbon capture and storage (CCS) would contribute considerably towards climate change mitigation, if it would be implemented on a very large scale; at many storage sites with substantial injection rates. Achieving high injection rates in deep saline aquifers requires a detailed assessment of injectivity performance and evaluation of the processes that alter the permeability of the near-well region. One of the most common forms of the injectivity loss in the context of CO_2 storage in saline aquifers is salt precipitation driven by the evaporation of brine into the relatively dry injected CO_2 stream. We present a novel compositional transport formulation based on overall-composition variables which models salt as a separate solid phase which could potentially form through two essentially different ways, *i.e.,* kinetic or equilibrium. To model formation drying-out and subsequent halite-precipitation, an accurate and reliable fluid model ePC-SAFT, which can effectively account for ionic effects, is applied. In addition, a volume balance approach (*i.e.,* depending on how far the salt saturation is from the solubility limit) is implemented to estimate solid saturation in a simulation cell. The resulting simulator is benchmarked against several well-known examples, with analytical solutions demonstrating the ability of the code to cover a variety of physical mechanisms. Finally, injection of dry CO_2 into a brine-saturated core-scale domain is simulated and sensitivity analyses over various parameters are performed. We show that the new model is capable to quantitatively represent the physics of salt precipitation (for example salt self-enhancing) under different reservoir conditions.

1. Introduction

Deep saline aquifers are considered as the most promising option for CO_2 sequestration to mitigate climate changes caused by increasing anthropogenic CO_2 in the atmosphere. The storage capacity of deep saline aquifers is huge (~2,000–20,000 Gt CO_2 (Bachu and Adams, 2003)), but the annual world-wide energy-related greenhouse-gas emissions are also large (~ 33 Gt CO_2 in 2018) and the need for reduction is imminent. This means that CO_2 storage will achieve significant climate change mitigation, only if it be implemented on a very large scale with considerable injection rates (in the order of 10 Mt CO_2/year). Achieving such high rates in deep saline aquifers requires a detailed assessment of injectivity performance and evaluation of the processes that alters the permeability of the near-well region. CO_2 is not an inert gas and its physiochemical interactions with the formation water may lead to injectivity decline. When injecting large volumes of under-saturated, supercritical CO_2 into a saline aquifer, formation water will evaporate and build up the concentration of dissolved salt in the brine. When the salt concentration exceeds its solubility limit under the thermodynamic state of a given reservoir, the excess salt will precipitate out of the aqueous phase and immediately alter the porosity and permeability of the reservoir (Miri et al., 2015; Miri and Hellevang, 2016).

There are several field evidences on the occurrence of salt precipitation during production/injection from gas reservoirs and during storage of natural gas (Bette and Heinemann, 1989; Kleinitz et al., 2003; Maxwell and Keith, 2014; Zhang and Isaj, 2015). In addition, the extra pressure build-up and loss of injectivity in the Ketzin (Baumann et al., 2014) and Snøhvit (Grude et al., 2014) CO_2 storage projects is also explained by this phenomenon. The macro-scale core flooding (André et al., 2014; Bacci et al., 2013, 2011; Ott et al., 2013, 2012, 2011; Peysson, 2012; Wang and Liu, 2013) and pore-scale microfluidic (Kim et al., 2013; Miri et al., 2015; Nooraiepour et al., 2018) experimental setups have often been used to explore physics behind

* Corresponding author.
E-mail address: rohaldinmiri@iust.ac.ir (R. Miri).

https://doi.org/10.1016/j.ijggc.2020.103075
Received 15 November 2019; Received in revised form 20 May 2020; Accepted 21 May 2020
Available online 17 June 2020

evaporation and consequent precipitation.

A review of these experiments shows that evaporation does not necessarily happen just at the flooding front (corresponding to the immiscible two-phase interface), but rather as a separate evaporation front, which may form and progress into the porous medium. This is a consequence of interplay between several physical mechanisms acting on different time and length scales.

It is challenging to predict the macroscopic distribution (*i.e.* the progression of the drying-out zone and the average porosity reduction) of the precipitated substances and the extent of formation damage. This is, however, necessary in order to deal with salt precipitation problems and to plan injection operations.

The majority of existing numerical codes which are capable to simulate the process of drying-out and salting-out (e.g. TOUGH2 (Pruess, 1991), DUMUX (Flemisch et al., 2011), CMG, and Eclipse), have been established based on implementing the physical process including: (1) immiscible two phase displacement, (2) brine evaporation into the dry CO_2 stream and (3) capillary-driven backflow of the aqueous phase. Previous studies have provided conflicting results on how salt precipitation impacts the static and dynamic properties of porous media. This is mainly due to lack of a sound physical dynamic flow model for a system containing salt phase. A detailed list of these discrepancies is provided in Miri and Hellevang (2016). It is likely that the contradicting results arise as some physical processes such as salting-out (owing to the implementation of weak equation of states), salt self-enhancing, and advection of the salt phase, have been either ignored or demonstrated via simple approaches in the existing numerical models. Therefore, the model representation of dynamic salt precipitation needs to be revised.

Pore-scale observations from our recent study (Miri et al., 2015) suggested two forms of salt crystallization by which salt precipitates out of aqueous phase. The first form involves relatively large, single crystals growing in the aqueous phase, specifically at low injection rates (*i.e.,* low evaporation rate) when the salt crystals have sufficient time to grow before liquid thinning begins. The second form involves the growth of aggregates of micro-meter size salt crystals in the CO_2 stream. These crystals, in both forms, can adsorb onto the rock surface, block the pore throats and thus reduce the CO_2 transmissibility.

The aim of this study has been to develop an improved model for simulation of salt precipitation and deposition in saline aquifers during CO_2 injection. This model provides a tool for evaluating dynamic effects of salting out on reservoir quality, and estimating effects of measures to prevent injectivity loss. Overall, such assessments are essential as part of risk evaluations and to ensure safe and sustainable storage of CO_2. To achieve this, in-house MATLAB simulation software, MRST, (Bao et al., 2017; Lie et al., 2007) is extended with a novel compositional transport formulation, based on overall-composition variables, which models salt as a separate solid phase growing and filling pore space through two essentially different, yet potentially contemporaneous mechanisms, i.e., kinetic or equilibrium. AD-MRST (automatic differentiation) is very flexible and applicable to general grids (e.g. refinement around the wellbore) and offers various types of grid coarsening (e.g. communicating pore volume to capture the regional pressure build-up) as well as state-of-the-art, multiscale methods which can be applied to make the simulations more efficient.

To model formation drying-out and subsequent halite-precipitation, an accurate and reliable fluid model, electrolyte version of perturbed chain statistical associated fluid theory (ePC-SAFT), which can effectively account for ionic effects, is used. To account for more complex processes, like the self-enhancing salt nucleation and precipitation mechanism described in Miri et al. (2015), the capillary pressure of the cells with solid is modified with a weight factor. In addition, different clogging models (*i.e.,* the relationships between permeability and effective porosity) are tested to predict the amount and distribution of halite-precipitates in the reservoir.

In the following, we will review the basic models for evaporation (using ePC-SAFT equation of state), salt precipitation, and multiphase flash calculations. We then introduce modifications toward compositional flow equations of the MRST software. Then, the resulting simulator is benchmarked against several well-known examples, with analytical solutions demonstrating the ability of the code to cover a variety of physiochemical mechanisms. To sum-up, we have simulated CO_2 injection into a one-dimensional core-scale domain, performed sensitivity analysis on important factor, and discussed the findings.

2. Model description

In this section, we will describe formulations for phase equilibria calculation, physical assumptions, and treatment of solid phase, which are built as an extension of a general ad-compositional model.

2.1. Water evaporation model

An accurate determination of components distribution among different phases is a very important step in modelling of different physical phenomena underlying a typical Carbon Capture and Storage (CCS) project. Among these, CO_2 concentration in water and water content of CO_2 have a superior priority as the former directly creates the so-called salting-out effect and the latter accelerates salt precipitation. However, a system such as H_2O–CO_2–Salt represents a complex fluid type due to highly non-ideal intermolecular interactions, such as association (hydrogen bonding), polarity, ionic bonds, and chain forming reactions. From thermodynamic modelling prospective, it is not trivial to estimate the exact location of the phase boundaries and components distribution of such a complex system, by using standard engineering equations-of-state of the Van der Waals type (Peng–Robinson, Soave-Redlich-Kwong a.o.). To account for these non-ideal interactions, the best alternative is incorporating a predictive thermodynamic model that considers additional interactions (forces) between molecules: Statistical Association Fluid Theory (SAFT) (Gross and Sadowski, 2002; Miri et al., 2014).

SAFT is a promising framework built on a reference term, which – unlike Van der Waals equations – can capture chain length (molecular shape) and molecular association (Chapman et al., 1989). Because of its accuracy and predictive capabilities, we used ePC-SAFT (Cameretti et al., 2005; Held et al., 2014; Ji et al., 2012) version of this theory to predict phase partitioning. SAFT treats the molecules as a chain composed of (m) spherical segments of equal size, bonded tangentially together and interacting via an intermolecular potential, *i.e.* Lennard–-Jones (LJ), square-well (SW) etc. SAFT-type equations-of-state are usually formulated in term of residual Helmholtz energy. Considering various type of molecular interactions, this energy is defined as:

$$\tilde{a}^{res} = \tilde{a}^{hc} + \tilde{a}^{disp} + \tilde{a}^{assoc} + \tilde{a}^{ionic} \tag{1}$$

Where $\tilde{a}^{res}$ is the difference between the total Helmholtz energy per mole and the ideal gas Helmholtz energy per mole at the same temperature and density. The superscripts refer to terms accounting for the hard-chain, dispersion, association, and ionic interactions, respectively. The formulation used for ionic contribution is provided in Appendix A-1. All other thermodynamic properties can be estimated through Helmholtz free energy. The fugacity coefficient, ϕ, of the components can be calculated through derivatives of residual Helmholtz energy respect to compositions as:

$$\ln \phi_i = \tilde{a}^{res} + \left(\frac{\partial \tilde{a}^{res}}{\partial x_i}\right)_{T,\rho,x_{j\neq i}} - \sum_{j=1} \left[x_j \left(\frac{\partial \tilde{a}^{res}}{\partial x_j}\right)_{T,\rho,x_{k\neq j}} \right] + Z - 1 - \ln Z \tag{2}$$

where x_i is the mole fraction of component i, T is temperature, ρ is density, and Z is compressibility factor and calculated with

$$Z = 1 + \rho \left(\frac{\partial \tilde{a}^{res}}{\partial \rho}\right)_{T,x} \tag{3}$$

The derivatives of residual Helmholtz energy with respect to density can be calculated both numerically and also analytically (here we used analytical derivatives). However, we noticed that derivatives with respect to compositions are highly sensitive, and we therefore recommend analytical derivation for them. The analytical derivation for hard chain and dispersion contribution of free Helmholtz energy can be found in Gross and Sadowski (2001), Mohebbinia (2013), Privat et al. (2010), for association contribution with respect to density can be found in Chapman et al. (1990). We provided the rest of the derivatives which are not available in the literature in Appendix A.

The model requires three parameters for each compound, namely: m, the number of segments, σ, the segment diameter, and ε, the segment energy. For associative molecules, two additional parameters are needed, the association volume, κ^{AB}, and the well depth of the association energy, ε^{AB}. We developed the thermodynamic package of this study based on the following considerations:

- It is assumed that the association term can capture the polarity contribution of the molecules.
- The ePC-SAFT considers the hydrogen bonding through cross association between unlike sites (i.e., O—H).
- The model for water molecules is based on the two-site single segment model proposed by Cameretti et al. (2005), in which two associating sites of type (H) and type (O) represent the proton-donor sites and electron lone pairs, respectively. Two sites of the same type (i.e., O–O or H–H) do not associate.
- CO_2 is not considered as an associative molecule.
- Dispersion interaction is not considered between ions (Cameretti et al., 2005).
- Three phases are modeled; the gaseous (G), aqueous (Aq), and solid phase (S).
- Aqueous phase contains H_2O, CO_2, Na^+, and Cl^-. Gaseous phase can contain H_2O and CO_2 (it is assumed that salt only dissolves in the aqueous phase). Solid phase only contains NaCl.

Since ePC-SAFT treats the ions as different components, we used Eq. (4) to calculate the fugacity coefficient of salt in the aqueous phase, as suggested by Tan et al. (2005).

$$\ln \phi_i = \ln \left(\phi_+^{\nu_+} \phi_-^{\nu_-}\right)^{\frac{1}{\nu_+ + \nu_-}} \tag{4}$$

Where ν_i is the stoichiometric coefficient of ion i. In our case $\nu_{Na^+} = \nu_{Cl^-} = 1$.

PC-SAFT parameters for water, Na^+, and Cl^- are taken from work of Cameretti et al. (2005). PC-SAFT parameters for CO_2 are taken from original PC-SAFT paper published by Gross and Sadowski (2001). PC-SAFT parameters for all the components are reported in Table 1.

The electrolyte and association contribution of the developed model are benchmarked for water-salt systems reported in Cameretti et al. (2005) and associative binary systems reported in Gross and Sadowski (2002). However, since no binary interaction parameters is reported for H_2O—CO_2—NaCl system in the literature, we used the interaction parameters reported in Table 2 to match the experimental data reported by Spycher et al. (2003), Yan et al. (2011). It is worth mentioning that, chemical reactions and kinetics associated with mutual solubility of water in vapour phase and gases in the liquid phase are not our concern here.

Table 2
Binary interaction parameters for $H_2O - CO_2$–NaCl system.

Component	H_2O	CO_2	Na^+	Cl^-
H_2O	0.0000	−0.010	0.0000	0.0020
CO_2		0.0000	0.3500	0.3500
Na^+			0.0000	0.0000
Cl^-				0.0000

2.2. Phase partitioning and stability analysis

Given a pressure P, a temperature T, and a mixture with global composition z, multi-phase flash calculations (vapour–liquid (V–L), liquid–solid (L–S) and vapour–liquid–solid (V–LL–S)) are performed to compute the phase fraction and the distribution of the components. Prior to flash calculations, number of phases in equilibrium is determined by applying the phase stability analysis using Gibbs free energy minimization (the stationary point criterion introduced by Michelsen (1982)). Phase equilibrium calculation procedures are established for systems where all existing phases could thermodynamically be described with an equation of state. The equilibrium state for such a system is as follows:

$$f_i^F = f_i^j \tag{5}$$

Where, f_i^j is fugacity of component i in phase j and F is the reference phase (commonly the light liquid phase).

The detailed procedure of phase equilibria calculations (stability analysis and multiphase flash calculations) for such a system can be found in our previous publication (Masoudi et al., 2020).

However, in the particular case of carbon storage in a saline aquifer, we cannot use the equilibrium state of Eq. (5) if we consider salt as a pure solid phase (i.e., with respect to CO_2 and water). The condition for thermodynamic equilibrium of this system is described with the following equations:

$$f_i^{aq} = f_i^G \text{ and } i = H_2O \text{ and } CO_2 \tag{6}$$

$$f_i^{aq} = f_i^S \text{ and} i = \text{salt} \tag{7}$$

where superscripts of aq, G, and S stand for aqueous, gaseous, and solid phase, respectively.

The fugacity of solid salt cannot be directly modeled with ePC-SAFT equation of state.

In this paper, we used a simple yet accurate method to calculate the fugacity of pure solid salt as described in the following:

Considering the thermodynamic equilibrium condition of Eq. (7), the fugacity of solid salt, f_{salt}^S, and the dissolved salt in aqueous phase, f_{salt}^{aq}, are equal at the saturation point. As we mentioned, the fugacity of the pure solid salt cannot be modelled directly with an equation of state. However, one can calculate the fugacity of the dissolved salt in aqueous phase with equation of states knowing the pressure, temperature, and composition of the solution at saturation point. Therefore, we used the SoWat code (Driesner, 2007; Driesner and Heinrich, 2007) to extract the composition of salt in the aqueous phase at saturation point in the range of 10 °C–90 °C and 1–500 MPa. We used the extracted data as inputs and calculate the f_{salt}^{aq} by the use of ePC-SAFT. Eq. (8) presents the best fit (in a least-squares sense) of f_{NaCl}^S to Temperature

Table 1
ePC-SAFT parameters for H_2O, CO_2, and ions.

Molecule/ Parameter	m	σ (Å)	ε/k (K)	κ^{AB}	ε^{AB}/k(K)
H_2O (Cameretti et al., 2005)	1.09528	2.8898	365.956	0.034868	2515.671
CO_2 (Gross and Sadowski, 2001)	2.0729	2.7852	169.21	0	0
Na + (Cameretti et al., 2005)	1	1.6262	119.806	0	0
Cl^- (Cameretti et al., 2005)	1	3.5991	359.6604	0	0

(K) and Pressure (Pa).

$$f_{NaCl}^{S} = -3.998 \times 10^{6} + 8975 \times T - 5642 \times \left(\frac{P}{10^{5}}\right) + 46.9 \times T^{2} + 28.74 \times T \times \left(\frac{P}{10^{5}}\right) \quad (8)$$

The fugacity of salt can also be calculated from an alternative thermodynamic cycle passing through melting point of pure salt as follows:

$$\ln\left(\frac{f_{salt}^{0,L}}{f_{salt}^{0,S}}\right) = \frac{\Delta H_m}{RT_m}\left(\frac{T_m}{T} - 1\right) + \frac{\Delta C_p}{R}\left(1 - \frac{T_m}{T}\right) - \frac{\Delta C_p}{R}\left(\frac{T}{T_m}\right) + \frac{\Delta V}{RT}(P - P^{sat}) \quad (9)$$

In Eq. (9), $f_{salt}^{0,L}$ and $f_{salt}^{0,S}$ are the fugacity of pure salt at subcooled liquid and solid phases respectively, ΔV is the molar volume difference of pure salt at liquid and solid phases, ΔH_m melting-point enthalpy of fusion, T_m is melting temperature, P^{sat} is the salt saturation pressure at its melting temperature, ΔC_P is the difference of heat capacities of pure salt at liquid and solid phases, and R is the universal gas constant. The second and third terms in Eq. (9) have opposite signs and they approximately cancel out each other. The last term accounts for pressure effects and can be ignored at low pressures. Therefore, the fugacity of the subcooled salt liquid can be calculated using Eq. (10).

$$\ln\left(\frac{f_{salt}^{0,L}}{f_{salt}^{0,S}}\right) = \frac{\Delta H_m}{RT_m}\left(\frac{T_m}{T} - 1\right) + \frac{\Delta V}{RT}(P - P^{sat}) \quad (10)$$

All the methods must get similar results.

Phase stability analysis for two phase gas–liquid system is solved using the quasi-Newton successive-substitution (QNSS) method, which is described in details by Nghiem and Li (1984). For salt to precipitate out of the system, fugacity of the salt in the aqueous phase must be larger than the fugacity of pure salt at same thermodynamic state ($f_{salt}^{aq} > f_{salt}^{S}$).

To perform multiphase flash calculations, the Rachford–Rice equation (Rachford and Rice, 1952) is modified to account for the solid phase as follows:

$$\sum_{i=1}^{N_c} \frac{(K_{iG} - 1)z_i}{1 + F_G(K_{iG} - 1) + F_S(K_{iS} - 1)} = 0 \quad (11)$$

Where N_C is the number of components, F_j is the molar phase fraction of phase j and K_{ij} is the equilibrium constant of component i with respect to phase j. K_{ij} is defined as:

$$K_{iG} = x_{iG}/x_{i,aq} \text{ and } x_{i,aq} = \frac{z_i}{1 + F_G(K_{iG} - 1) + F_S(K_{iS} - 1)}$$
$$K_{iS} = x_{iS}/x_{i,aq} = \begin{cases} 0 & i = 1,\ldots,N_c \\ 1/x_{salt,aq} \end{cases} \quad (12)$$

Rachford-Rice equations are solved using the analytical Jacobians obtained by automatic differentiation (AD) feature of MRST. We also developed another solver using bisection method for the cases that the previous method cannot solve the set of nonlinear equations, for example near the phase transition zones, where Fj →1 or Fj →0.

2.3. Flow model based on overall-composition variables

The computational domain considered in this study consists of three phases (liquid, gas, and solid). The mass conservation based on the overall composition formulation is given by:

$$\frac{\partial}{\partial t}(\varphi \rho_t z_i) + \nabla .\ L + q_i^W = 0 \quad (13)$$

where ρ_t denotes the total density, φ is porosity and q_i^w denotes the well rate of component i in $[mol/m^3/s]$. z_i can be presented by following equation:

$$z_i = \frac{\sum_{j=1}^{N_p} \rho_j S_j x_{ij}}{\sum_{j=1}^{N_p} \rho_j S_j} = \sum_{j=1}^{N_p} F_j x_{ij} \quad (14)$$

Where N_p is the number of phases, S_j saturation of phase j, F_i mole fraction of phase j, x_{ij} composition of component i in the phase j. The flux term, L, is presented as follows:

$$L = \sum_{j=1}^{N_p} (\rho_j x_{ij} u_j - \varphi \rho_j S_j \boldsymbol{D}_{ij} \nabla x_{ij}) \quad (15)$$

Where $\boldsymbol{D_{ij}}$ denotes dispersion tensor and u_j is phase velocity described with the Darcy's law:

$$u_j = -K\lambda_j(\nabla P_j - \rho_j g \Delta h),\ \ \lambda_j = \frac{k_{rj}}{\mu_j} \quad (16)$$

where K is permeability tensor; k_{rj} is the relative permeability of phase j, which is a function of the phase saturation, λ_j phase mobility, μ_j viscosity of phase j, Δh is height difference and g is the magnitude of gravity in the vertical direction. The capillary is calculated by following equation:

$$P_j = P_L - P_c^j \quad (17)$$

P_L is pressure of the reference phase (liquid), P_j is the pressure of phase j, and P_c^j is capillary pressure of phase j. We used the relations listed in Table 3 for capillary pressure and relative permeability.

2.4. Salt precipitation model

The mass conservation for salt species given by Eq. (13) is not complete as it lacks the mass of deposited salt. To resolve this, a source term, (q_{salt}), representing the mass of deposited salt is added to the right-hand side of Eq. (13) for fluid species other than CO_2 and H_2O.

$$q_{salt} = \frac{\partial}{\partial t}(V_{salt}\, \rho_{S,salt}^{mol}) \quad (18)$$

Where V_{Salt} is the volume of precipitated salt in each grid block and $\rho_{S,Salt}^{mol}$ is the molar volume of solid salt. This source term represents the transfer of salt species between aqueous and solid phase. There are two methods to calculate this transfer function. In the first approach, which is referred to as the equilibrium approach, we estimate the volume of precipitated salt directly from the flash calculations. This will be achieved if fugacity of the salt in the aqueous phase be larger than the fugacity of pure salt at same thermodynamic state ($f_{salt}^{aq} > f_{salt}^{S}$). In the second approach, precipitation and dissolution of salt is considered as kinetic reaction follows as:

$$q_{salt} = k_{salt}\varphi \rho_L^{mol} S_L (x_{salt} - x_{salt,\max}) \quad (19)$$

where k_{salt} is the reaction rate constant with units of time^{-1} and $\rho_{L,Salt}^{mol}$ is the molar volume of liquid. It can be a positive number corresponding to deposition or a negative value for dissolution. When salt reaches its

Table 3
Relative permeability and capillary pressure functions used in this work.

Parameters	Value
Capillary pressure Brooks-Corey relation, P_{cwg}	$P_{cwg}(S_w) = P_{ct}(\frac{1 - S_{wr}}{S_w - S_{wr}})^{1/\lambda}$
Normal water saturation, S_{wn}	$S_{wn} = \frac{S_w - S_{wr}}{1 - S_{wr} - S_{gr}}$
Water relative permeability, K_{rw}	$k^{rw}(S^{wn}) = k_{rw}^{*}(1 - S^{wn})^{n_w}$
Gas relative permeability, K_{rg}	$k^{rg}(S^{wn}) = k_{rg}^{*}(1 - S^{wn})^{n_g}$
Water relative permeability endpoint, K_{rw}*	1
Gas relative permeability endpoint, K_{rg}*	1
Water relative permeability exponent, n_w	2
gas relative permeability exponent, n_g	2
Threshold capillary pressure, P_{ct}	0.25 MPa
Exponent in Brooks-Corey, λ	2

maximum solubility limit, $x_{salt,\max}$, it will precipitate instantaneously. In addition, in the presence of fresh water, the deposited phase readily and rapidly re-dissolve to the extent possible.

The porosity reduction due to salt precipitation can be simply calculated using following equation:

$$\varphi = \varphi_0 - S_S \tag{20}$$

Where the φ_0 initial porosity and S_S is the salt saturation defined as the volume of the deposited salt per unit volume of a grid block.

2.5. Well equations

The source term, q_i^W, accounts for the presence of a component in the different phases, with the phase-volume-source terms determined by the standard (Peaceman, 1983) model:

$$q_i^W = \sum_{j=1}^{N_p} \rho_j x_{ij} \boldsymbol{q}_{ij} \tag{21}$$

and $\boldsymbol{q}_{ij}$ for a producing well is

$$\boldsymbol{q}_{ij} = T_{prod} \lambda_j (P - P_{bh} - g\rho_m \Delta h_w) \tag{22}$$

where T_{prod} is the productivity index, P_{bh} is bottom hole pressure, and the $g\rho_m \Delta h_w$ term represents the hydrostatic pressure drop due to height difference, Δh_w, between perforations and blocks.

2.6. Overall computational procedure

The system of equations described in the previous sections were solved simultaneously using the Newton's method. The primary variables of Eq. (13) are pressure, P, and overall composition, z_i, in addition to a set of well variables, resulting in n_{pr} unknowns (n_{pr} denotes the number of primary unknowns). The remaining set of variables including the remaining overall composition, phase molar fractions, and fluid phase compositions, forms the secondary unknowns n_{sec}. However, distribution of component in each phase is required to calculate parameters in Eq. (13). The distributions of composition in addition to saturations can be calculated using thermodynamic calculation and the following secondary equations:

$$\sum_{i=1}^{N_c} x_{ij} = 1, \quad j = 1, \ldots, N_p \tag{23}$$

$$\sum_{i=1}^{N_c} z_i - 1 = 0 \tag{24}$$

$$\sum_{i=1}^{N_p} F_i - 1 = 0 \tag{25}$$

The system of linearized equations (one for each component and cell/block) is solved using iterative Newton-Raphson method implemented in AD-MRST multiscale solver. In the fully-implicit scheme, the solution is computed for each time step as follows: In each Newton iteration, the global system of primary equations and variables is solved. Subsequently, the secondary, local equations are resolved on a grid-block basis for secondary variables, keeping the primary variables fixed. This is also interpreted as applying the flash algorithm, which entails finding the solution of small local nonlinear problems. Once the secondary equations are solved, all fluid and solid properties are updated. The overall computation procedure is depicted in the Fig. 1.

3. Model testing

In this section we examine the performance of the proposed model based on our fully-implicit implementation in AD-MRST. We validate the model in two parts: (1) thermodynamic package where flash calculations and stability analysis have been implemented and (2) the flow solver where new formulations have been proposed and implemented.

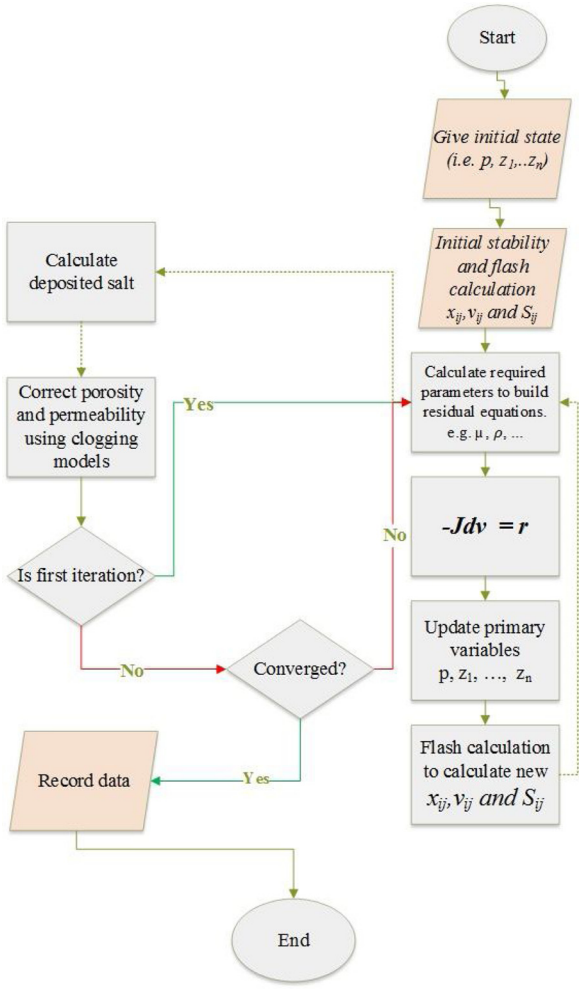

Fig. 1. Flow chart of overall composition considering deposition of salt for a single time step.

3.1. Thermodynamic package validation

To quantify the accuracy and the capability of the implemented thermodynamic package (*i.e.,* the equation of state and flash calculation procedure) in predicting phase partitioning of non-ideal components, a complex asphaltenic fluid is chosen as a test case. The reason for choosing this system is lack of experimental data on phase separation of CO_2-Brine system on a wide range of temperature and pressure. The chosen fluid has been tested by several researchers with various models evidencing soundness of the obtained experimental data. The composition and the parameters of ePC-SAFT for pure components of this fluid are shown in the Table 4. Comparison of the results of experimental data with numerical solution of the developed thermodynamic package model are presented in the Fig. 2. The simulation results are in good agreement with the experimental data confirming that the model is predictive. Fig. 3 shows the competence of the package to model phase behavior of CO_2-Brine system in a wide range of pressure and temperature relevant to the CO_2 storage in saline aquifers. The solubility of CO_2 in brine increases with pressure and decreases with temperature. Below the critical temperature, a sharp discontinuity can be observed for H_2O solubility in CO_2, which coincides with a phase change from a gaseous to a liquid CO_2-rich phase. When pressure increases, water evaporation into the gaseous CO_2-rich phase decreases but, on the contrary, water solubility in liquid CO_2 increases. Mutual solubility

Table 4
Pure component properties used in PC-SAFT EOS of the asphaltenic crude used for thermodynamic package validation.

Components	Composition	MW (g/mol)	T_c (°R)	P_c	ω	m	σ	ε/k
N_2	0.00495	28.014	227.490	492.31	0.04000	1.2050	3.3130	90.96
CO_2	0.14583	44.010	548.790	1071.3	0.22500	2.0730	2.7850	169.21
C_1	0.27334	16.043	343.410	667.97	0.01300	1.0000	3.7040	150.03
Light	0.21917	44.600	665.970	615.76	0.15240	2.0546	3.6130	204.96
Saturate	0.23853	207.60	1346.45	263.89	0.67895	5.9670	3.9320	254.05
Aro-Res	0.11750	270.50	1346.45	263.89	0.67895	6.4730	3.8700	332.52
Asphaltene	0.00068	1700.0	2242.30	110.97	2.07070	29.500	4.3000	392.56

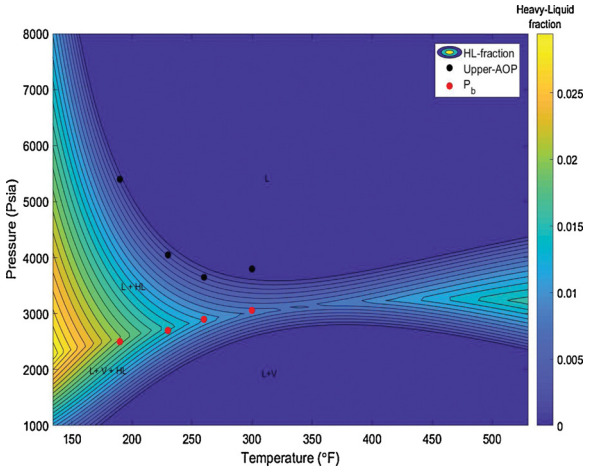

Fig. 2. Asphaltenic crude oil phase diagram obtained by the developed thermodynamic model. The solid black dots show the experimental upper onset pressure and red dots are bubble point pressure. (For interpretation of the references to color in this figure legend, the reader is referred to the web version of this article.)

decreases with salinity, although it is more noticeable for CO_2 solubility in brine.

3.2. Flow model validation

To test the ability of the implemented code in undertaking various physics, extensive validation on the flow model is performed. The chosen test cases have a wide range of complexity from simple single-phase flow to more complex three-phase problems. We compare the simulation results were compared with the analytical solution. The test cases include: (1) one dimensional mass diffusion, (2) one dimensional two-phase immiscible displacement i.e., the well-known Buckley-Leverett problem, (3) the free fall gravity drainage in the gas invaded zone of naturally fractured reservoirs and (4) the counter current imbibition in the water invaded zone of naturally fractured reservoirs. These problems simulate diffusion, gravity and capillary dominated process.

Table 5
Model parameters used in simulation of pressure diffusivity (Case A).

Parameter	Value
Permeability, k *(mD)*	100
Porosity, φ	0.20
Length, l, [m]	1000
Initial pressure (MPa)	13.79
Boundary pressure (MPa)	17.24

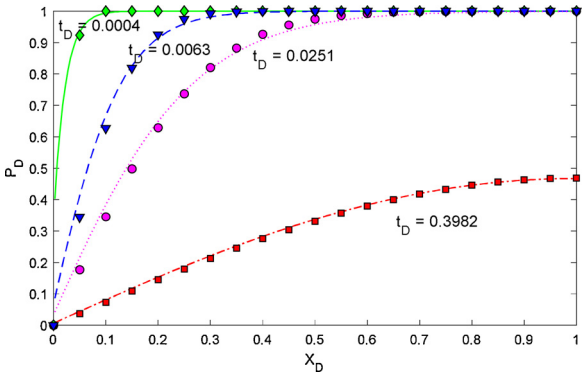

Fig. 4. Comparison between analytical solution (lines) and simulated results (symbols) of pressure diffusivity in Case A.

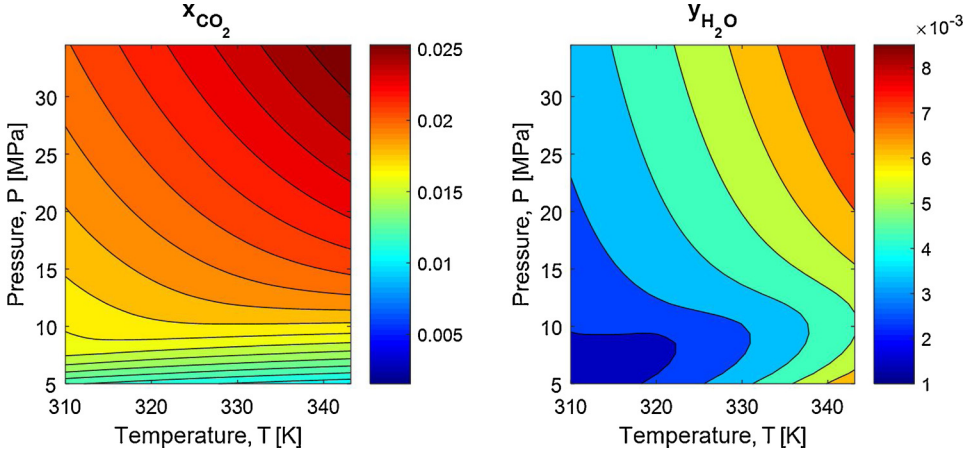

Fig. 3. Solubility of CO_2 in water (left) and solubility of water in CO_2 phase (right) for different pressures and temperatures. Salinity of the brine is 4.5 molal.

Table 6
Model parameters used in simulation of Buckley-Leverett problem (Case B).

Parameter	Value
Porosity, φ	0.10
Permeability, k, [m^2]	4.50×10^{-13}
Length, l, [m]	320
Water injection rate, Q, [m^3/day]	12
Cross-sectional area, A, [m^2]	900
Length increments, ΔX, [m]	4
Time step, Δt, [s]	10^5

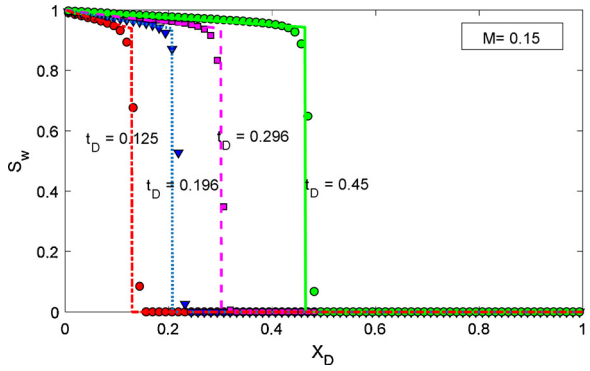

Fig. 5. Comparison between analytical (lines) and numerical solution (symbols) of Buckley-Leverett problem (Case B). The mobility ratio ($M = \frac{\lambda_{displacing}}{\lambda_{displaced}}$) for this case is 0.15.

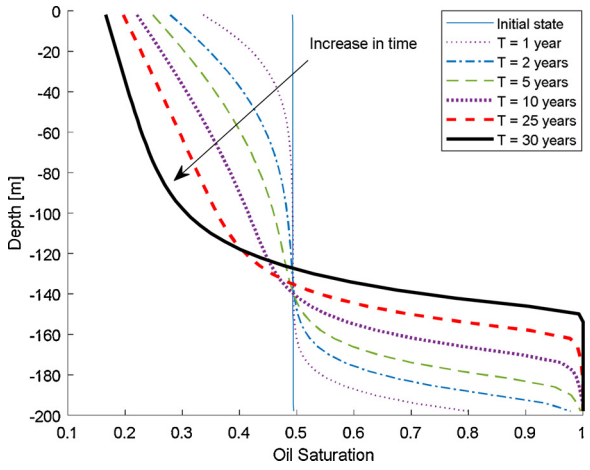

Fig. 6. Oil Saturation profile in the gravity drainage example (Case C).

3.2.1. Case A: Pressure diffusivity

The obtained flow model in the first step is validated by analytical solution for pressure diffusion in a one-dimension single phase flow. This simple fluid consists of methane, carbon-dioxide and n-decane. Grid structure for this case include 200 cells in x direction. Constant pressure boundary condition is applied at left side of the system and the rest of the boundary conditions are set as no flow. Other necessary data are summarized in the Table 5. The analytical solution of the diffusivity equation for this case is presented as (Hassanzadeh, 2006):

$$P_D = \frac{P - P_0}{P_i - P_0} = \sum_{n=1}^{\infty} \left(\frac{4}{(2n-1)\pi}\right) \exp\left[-\frac{(2n-1)^2 \pi^2 t_D}{4} \right] \sin\left(\frac{(2n-1)\pi X_D}{2}\right) \quad (26)$$

$$P_D(0, t_D) = 0 \quad (27)$$

Table 7
Model parameters used in simulation of counter-current imbibition problem (Case D).

Parameter	Value
Porosity, φ	0.10
Permeability, k, [m^2]	4.50×10^{-13}
Length, l, [m]	320
Water injection rate, Q, [m^3/day]	12
Cross-sectional area, A, [m^2]	900
Length increments, ΔX, [m]	4
Time step, Δt,[s]	10^5
Oil and water viscosity, μ, [cp]	1
Residual oil saturation	0.001
Irreducible water saturation	0.001
Water exponent	4
Oil exponent	4
Capillary pressure constant, b, [kPa]	10
Water end point and Oil end point	1

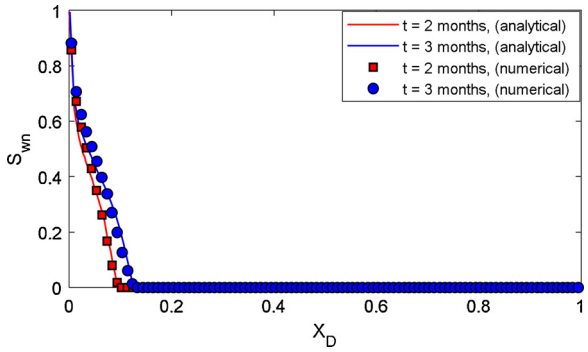

Fig. 7. Comparison between analytical (continuous lines) and numerical solution (open circles) of the counter-current imbibition problem (Case D). S_{wn} is normalized water saturation $S_{wn} = (\frac{S_w - S_{wr}}{1 - S_{wr} - S_{or}})$.

Table 8
Required data for Base Case.

Properties	Value
Number of grids	15 × 1 × 1
Lx, Ly, Lz	[15, 6, 6] cm
Constant pressure at outlet	80 MPa
Injection rate	25 cc/min
Fluid composition, [H_2O, CO_2, Na^+, Cl^-], mole fraction	[0.9068,0, 0.0466,0.0466]
Salinity	25 wt.%
Maximum salt solubility, $x_{salt,\max}$, mole fraction	0.1224
Initial Permeability	7.78 mD
Initial Porosity	0.2259
Residual water saturation, S_{wr}	0.35
Residual gas saturation, S_{gr}	0.10
Minimum water saturation, $S_{w,min}$	0.1
Temperature, T	338.15 K
Clogging model	Power-law

$$\frac{\partial P_D}{\partial X_D}(1, t_D) = 0, \quad (28)$$

$$t_D = \frac{kt}{l^2 \varphi \mu c_t} \text{ and } X_D = X/l \quad (29)$$

where P_D is dimensionless pressure, c_t is total compressibility factor, φ is porosity, X is distance, l is length, t_D is dimensionless time, t is time, and k is permeability. The simulated pressure distribution for this case at different dimensionless times is shown in the Fig. 4. The simulation results are in good agreement with the analytical solution approving competence of the code to simulate single-phase flow problems.

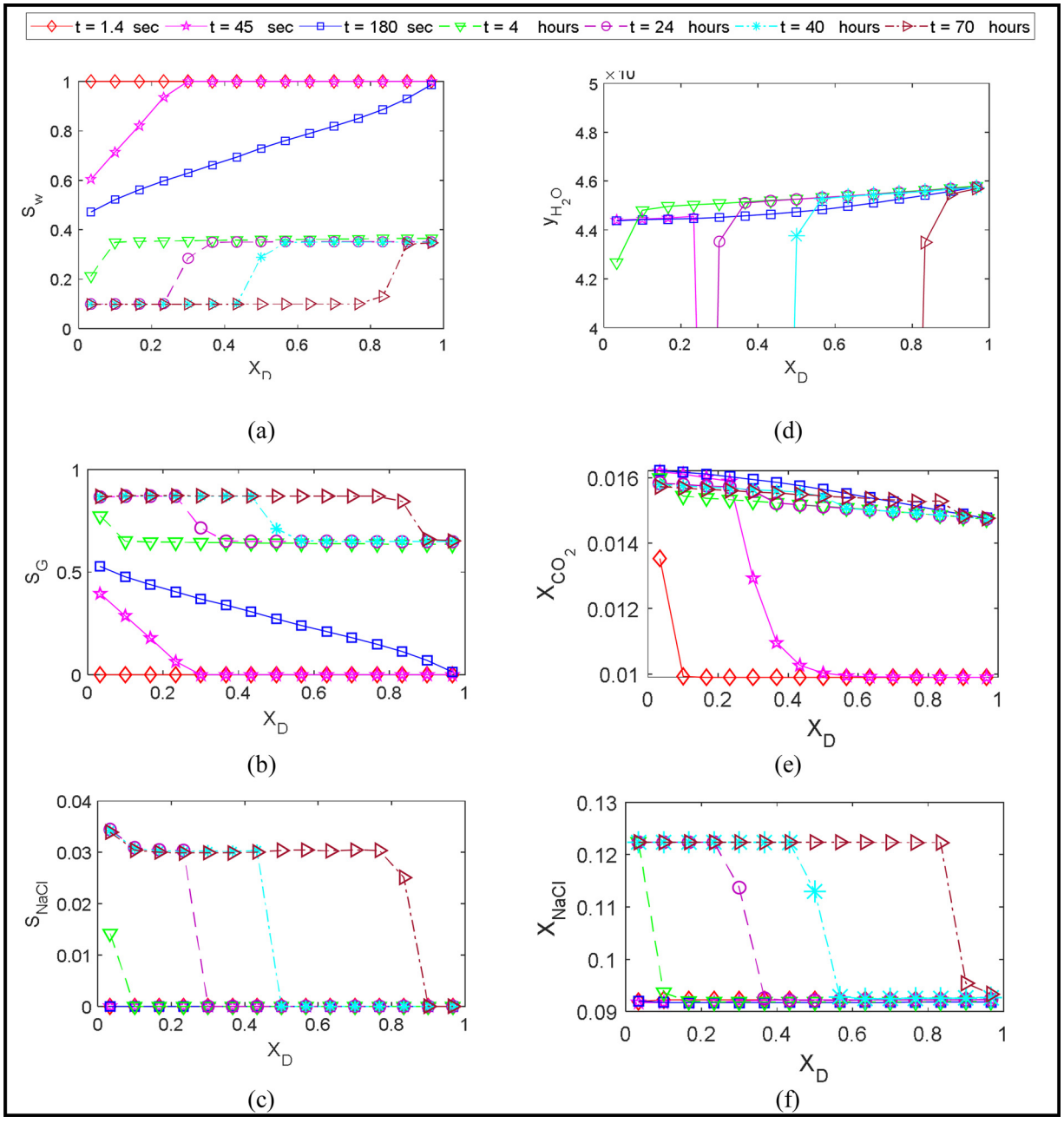

Fig. 8. Compositional core-scale simulation of salt precipitation via an equilibrium approach. Water, CO_2 and salt saturation and concentration along the core at different time steps during displacement of brine by CO_2 (Base Case, Q = 25 cc/min, Salinity = 25 wt%).

3.2.2. Case B: Buckley–Leverett problem

The Buckley–Leverett is a well-known conservation equation in reservoir engineering. It describes the displacement of two immiscible fluids (such as water and oil) in porous media (Buckley and Leverett, 1942). The Buckley–Leverett equation for one dimensional flow (Eq. (30)) is derived base on the assumptions such as homogenous and incompressible porous media, incompressible fluid, constant injection rate, constant fluid properties and insignificant capillary and gravity forces.

$$\frac{\partial S_w}{\partial t_D} + \frac{\partial f_w}{\partial X_D} = 0, \quad where\ f_w = \left[1 + \left(\frac{k_{rnw}}{k_{rw}}\right)\left(\frac{\mu_w}{\mu_{nw}}\right)\right]^{-1}$$
$$X_D = \frac{\varphi X}{l} \quad and \quad t_d = \frac{Qt}{A} \tag{30}$$

in Eq. (30), S_w is the wetting-phase saturation, φ is the rock porosity, X is distance, l is the length, Q is the total volumetric injection rate, t is time, f_w is water fractional flow, A is the area of the cross-section and k_{rw} and k_{rnw} are the wetting and non-wetting phase relative permeability, respectively. In this example, the k_{rw} and k_{rnw} are represented with the following equations:

$$k_{rw} = S_w^2 \tag{31}$$

$$k_{rnw} = (1 - S_w)^2 \tag{32}$$

It is assumed that the system is initially saturated with oil and the water is injected from the left side. Water displaces the oil with constant rate. The input data used in this case are summarized in Table 6. The front advancement is predicted using both approaches and shown in Fig. 5. The comparison shows that the obtained flow model gives acceptable results in two-phase flow systems.

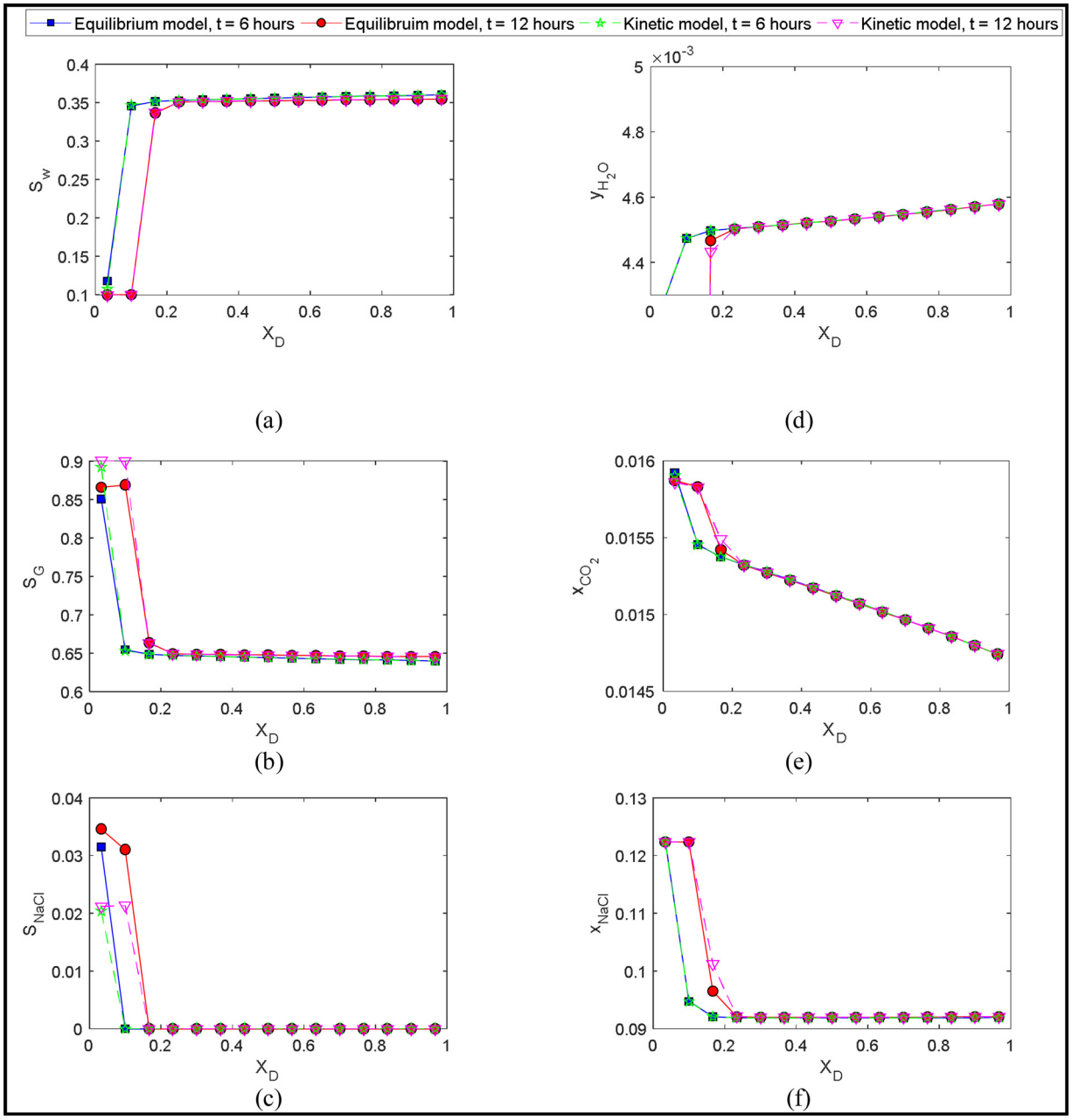

Fig. 9. Comparison of kinetic versus equilibrium approaches for salt precipitation. Water, CO_2 and salt saturation and concentration along the core at different time steps during displacement of brine by CO_2 (Base Case, Q = 25 cc/min, Salinity = 25 wt%).

Table 9
List of clogging models incorporated into the simulator.

Type	Reference	Model	Adjustable parameter
Verma–Pruess	Pruess and Müller (2009)	$\frac{k}{k_0} = \left(\frac{\phi/\phi_0 - \phi_r}{1-\phi_r}\right)^2$	$\phi_r = 0.9$
Kozeny–Carman	Zeidouni et al. (2009)	$\frac{k}{k_0} = \left(\frac{\phi}{\phi_0}\right)^3 \left(\frac{1-\phi_0}{1-\phi}\right)^2$	$\phi_0 = 0.2259$
Kozeny–Carman	Wang et al. (2010)	$\frac{k}{k_0} = \left(\frac{\phi}{\phi_0}\right)^c \left(\frac{1-\phi_0}{1-\phi}\right)^c$	$c = 2.4$
Power-law	Mohamed and Nasr-El-Din (2013)	$\frac{k}{k_0} = \left(\frac{\phi}{\phi_0}\right)^n$	$n = 5.17 - 448.2$ In this case $n = 10$

3.2.3. Case C: Gravity column

The free-fall gravity drainage is a production mechanism which occurs in gas-invaded zones of naturally fractured reservoirs (NFRs) where invaded gas from the gas cap surrounds oil-saturated matrix blocks. The immersed matrix blocks will drain if the gravity head created by the height of gas column in the adjacent fractures overcomes the capillary threshold height of the matrix blocks. In order to properly model this mechanism, the capillary pressure functions must be considered. In the previous version of the AD-MRST Compositional, the capillary pressure between oil and gas was ignored. To test the implementation of the capillary pressure, drainage of a gravity column is simulated. The fluid is the same as case A. There are two wells in this case: (1) the CO_2 injection well located at the top of the column and (2) the production well at the bottom of the column. Both wells are at the constant bottom-hole pressure. In this case, as oil is being produced due to gravity forces the oil saturation decreases at the top and increases at the bottom of the column. The saturation distribution in the column in different time is illustrated in Fig. 6. Oil production will last until the saturation profile in the column becomes similar to the equivalent

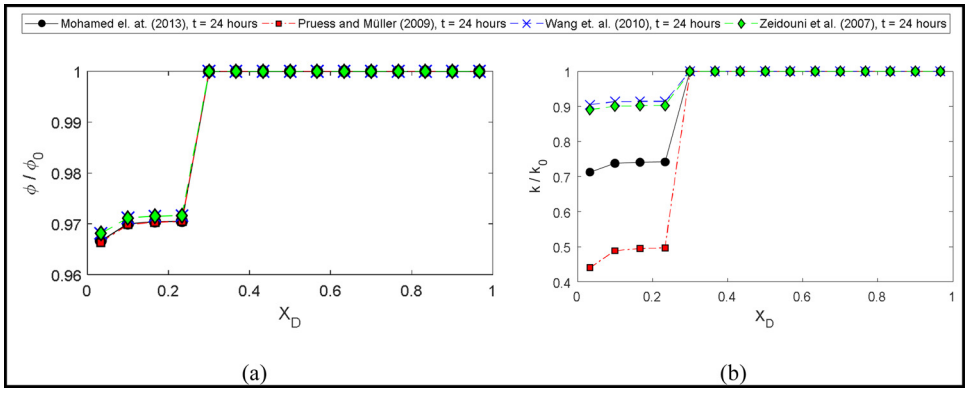

Fig. 10. Sensitivity analysis of various clogging models on temporal evolution of porosity and permeability along the core.

height of the capillary function (see Fig. 6). The results again demonstrate that the implemented multi-components multi-phase flow simulator can properly model the capillary pressure in a gravity dominated process.

3.2.4. Case D: Counter-current imbibition

Counter-current imbibition is a capillary dominated process where a wetting phase like water is sucked into a water-wet/mixed-wet porous media and drains out a non-wetting phase in opposite directions. This process significantly contributes to the oil production from the naturally fractured reservoirs and therefor it has been thoroughly studied in the literature. McWhorter and Sunada (1990) have offered a one-dimensional mathematical model for this process assuming incompressible rock and fluids properties:

$$\frac{\partial}{\partial X}\left(D(S_w)\frac{\partial S_w}{\partial X}\right) = \frac{\partial S_w}{\partial X} \tag{33}$$

Where D is the capillary diffusion function represented by following equation:

$$D(S_w) = -\frac{kk_{ro}}{\mu_o \varphi} f(S_w)\frac{dP_c}{dS_w} \tag{34}$$

here, μ_o is oil viscosity, In addition, the initial and boundary conditions are assumed as:

$$S_w(X, 0) = S_{wi} \quad t = 0 \quad 0 \le X \le l \tag{35}$$

$$S_w = 1 - S_{or} \quad t > 0 \quad X = 0 \tag{36}$$

$$q_w = 0 \quad t = 0 \quad x = l \tag{37}$$

q_w is water flow rate and other notations are already explained. The analytical solution of this problem is given in the Appendix B. In order to validate the obtained model, we assumed that a reservoir is initially saturated with oil and relative permeability and capillary pressure function are given as follows:

$$k_{rw} = k_{rw}^0 S^{n_w}, \ where \ S = \frac{S_w - S_{irw}}{1 - S_{irw} - S_{or}} \tag{38}$$

$$k_{ro} = k_{ro}^0 (1 - S)^{n_o} \tag{39}$$

$$P_c = b \ln S \tag{40}$$

The data used in numerical calculation are summarized in the Table 7. Comparison of the results of analytical solution (Equation B-2) with numerical solution using the developed compositional model are presented in the Fig. 7. The simulation results are in good agreement with the analytical solution.

4. Results and discussion

We consider a basic problem of CO_2 injection into a one-dimensional core-scale domain. The model represents a cube that is 15 cm × 6 cm × 6 cm. Flow is in the x-direction and a total of 15 grid blocks are used. CO_2 is injected into core plug with constant flux at the left side of the core and water is produced from the right side with constant pressure (8 MPa) boundary condition. The outlet is represented by a Dirichlet boundary of zero capillary pressure. The permeability is 7.78 mD, porosity is 22.59%, and the initial reservoir pressure is 80 MPa. The domain is initially saturated with NaCl brine. The salinity of the brine is 25% (250,000 ppm). The data for base case are presented in Table 8. The relations in Table 3 are used for capillary pressure and relative permeability.

Fig. 8 presents the results of our base case. The results show that just after the start of CO_2 injection, a two-phase-flow zone forms and progresses towards the core where both an aqueous phase and a CO_2-rich phase are present (Fig. 8-a and b). As a result of this two-phase immiscible displacement, brine flows out of the core until the residual water saturation (S_{wR}) of 0.35 is reached. This stage is very quick and occurs within 5 min after start of injection. Soon after, because the brine phase no longer flows, the drained region is exposed to the constant flow of dry supercritical CO_2 ($scCO_2$) with low water vapour pressure. This exposure initiates an evaporation regime, which increases the molar fraction of NaCl in water, causing halite deposition (Fig. 8-c to f). The water evaporates until it reaches minimum water saturation of 0.1.The dry-out front (or evaporation front as depicted in Fig. 8) is much slower than the flooding front (comparing the upper and lower parts of Fig. 8-a and b); therefore, most of the water mass exchange takes place in the dry-out zone. This will result in a homogenous salt distribution, corresponding to a *evaporative regime* as indicated in Miri and Hellevang (2016).

4.1. Sensitivity analysis on the governing parameters

Our earlier review study (Miri and Hellevang, 2016) of the performed numerical and experimental works on salt precipitation shows that the phenomenon is a complex process depending on several parameters, including thermodynamic conditions (pressure, temperature, salinity, composition of CO_2 and brine), injection scheme (injection rate, time frame), rock and fluid properties, and well completion scheme. In the following, sensitivity analyses are performed on some of the most challenging parameters.

4.2. Kinetic vs equilibrium deposition model

As mentioned previously (see Section 2.4 above), the developed model in this work can estimate the amount of deposited salt in each time step using either Kinetic or Equilibrium approaches. In the

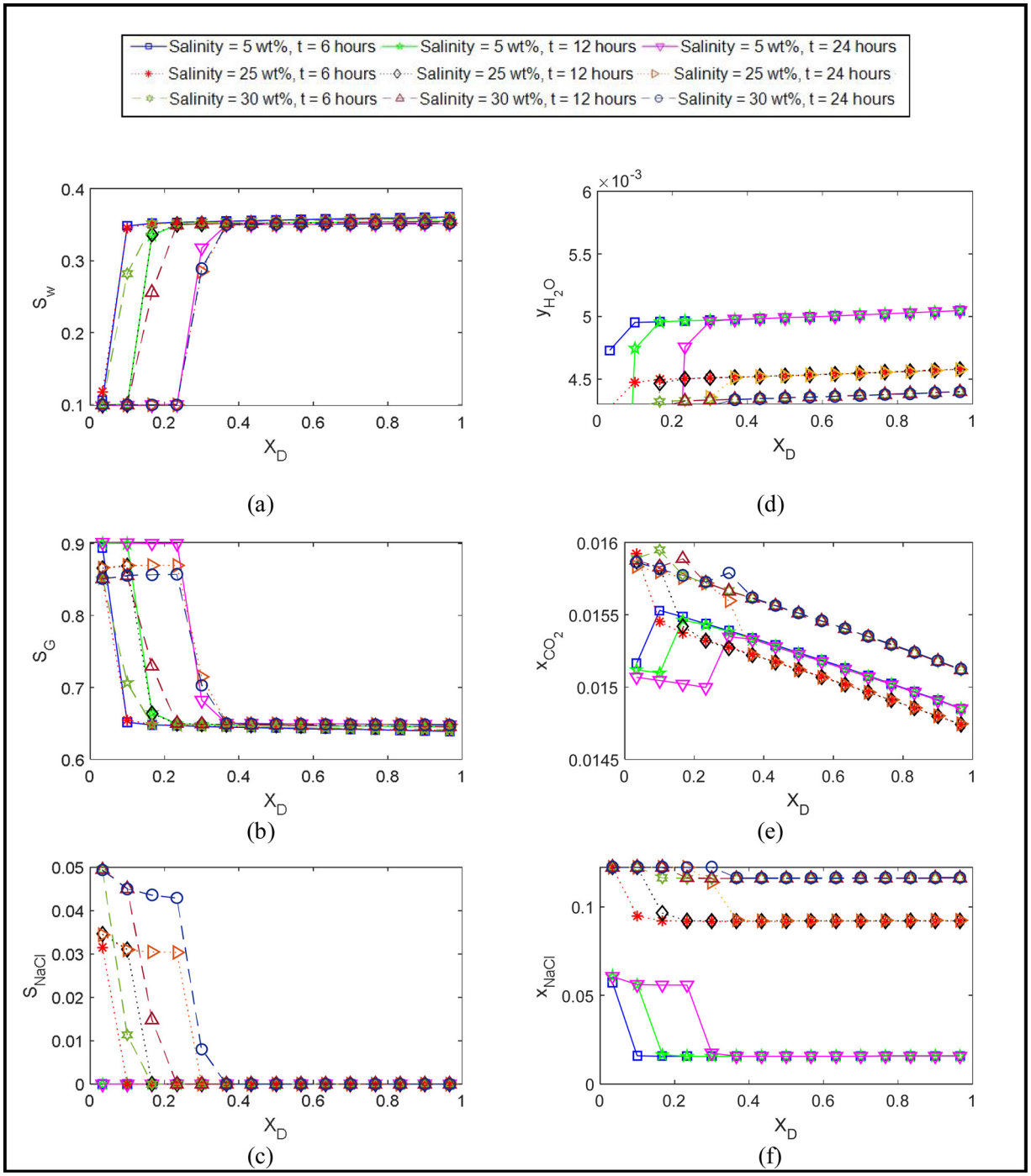

Fig. 11. Sensitivity analysis of salinity on Water, CO_2 and salt saturation and concentration along the core at different time steps during displacement of brine by CO_2 (Base Case, Q = 25 cc/min).

Equilibrium approach, salt instantaneously deposited when it reaches its solubility limit determined from ePC-SAFT. In addition, salt will be instantaneously dissolved back into brine in the presence of fresh water. In this approach, we assumed a third phase (salt phase) in the flash calculations which forms based on the Gibbs minimization stability analysis.

In the kinetic approach, however, reaction rate constants for dissolution and precipitation are equal. In this formulation, once the dissolved salt is precipitated out of the system, the aqueous phase composition needs to be scaled accordingly, which makes the flash calculations algorithm not as efficient and stable as the previous approach.

The results of comparison are depicted in Fig. 9. These two approaches give different results especially for the salt saturation where kinetic approach gives lower values. Roels et al. (2014) argued that the present-day numerical simulators (e.g. TOUGH2/ECO2N) predict heterogeneous salt accumulation near the inlet (for a diffusive drying regime where we normally expect a homogeneous distribution of precipitants) that is principally due to improper application of a local equilibrium phase partitioning. Our results support this statement; however, it turned out that for higher reaction rate constant ($\sim 10^3$), both approaches give similar results.

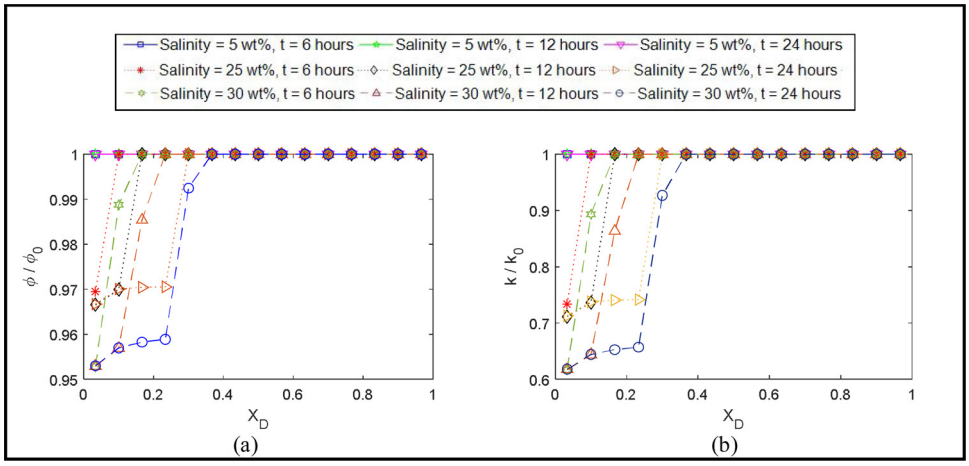

Fig. 12. Sensitivity analysis of salinity on temporal evolution of porosity and permeability along the core.

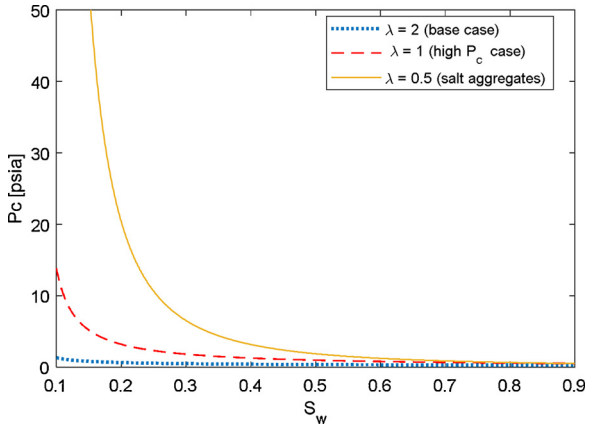

Fig. 13. Three sets of capillary pressure curves used for sensitivity analysis.

4.3. Clogging model

The clogging models define an intrinsic relation between porosity and permeability caused by alteration of pore morphology. In the reservoir simulation, the extent of formation damage and injectivity alteration is strongly controlled by clogging models irrespective of mechanisms occurring at pore scale. However, the microscopic pattern of the precipitated substances forms the basis for developing a proper clogging model. One can use various clogging models to model salt precipitation. Hommel et al. (2018) reviewed a variety of existing porosity-permeability relations and their essential features. Most of clogging models are built based on the homogenous layer of salt covering grain surfaces. The most popular model in this category is the one given by Verma and Pruess (1988), where a porous medium is conceptualized as a series of connected tubes of varying sizes.

We have done a sensitivity analysis on some of the most frequently used clogging models listed in Table 9 (Fig. 10). The results show that the flooding front and evaporation front location and velocity are not sensitive to the choice of clogging model, yet, the saturation of salt in dried zone is higher for power law and Verma and Pruess clogging models. In addition, as it is expected, Verma and Pruess clogging model gives utmost permeability reduction among all the other clogging model (Fig. 10).

4.4. Salinity

Salinity of the aquifer chiefly influences salt formation with controlling the onset and extent of precipitation. As it is shown in Fig. 3, increasing brine salinity causes a slight decrease of water solubility in the CO_2 phase, which in turn decreases the rate of evaporation. However, a noteworthy drop in the dissolution of CO_2 in the brine is observed. The sensitivity analysis on the salinity (Figs. 11 and 12) shows that higher salinity results in more salt precipitation and higher porosity reduction. However, for salinity less than 5% salt deposition and permeability impairment is negligible. These results are in good agreement with field observations. For example, for reservoirs of low salinity and high permeability, such as the Utsira Formation at the Sleipner Field in the North Sea (3.5% salinity and ~1 Darcy permeability), field observations of injectivity impairment or well clogging are not reported so far. However, for the Ketzin storage site, in a reservoir with high salinity (25%) and intermediate permeability (~100 mD) salt precipitation has been reported as the main reason for pressure build-up in the course of CO_2 injection (Grude et al., 2014).

4.5. Capillary pressure

One of the most significant parameters in the precipitation process is capillary pressure which primarily depends on pore-size distribution. A porous media with higher capillary pressure (*i.e.,* small pores) may increase the capillary back-flow, which could affect both macroscopic and microscopic distribution of deposited salt. It is generally accepted that capillary pressure serves to increase the rate of evaporation by supplying fresh brine to the drying front. To conduct sensitivity analysis on capillary pressure, we have implemented four sets of capillary pressure:

1 Zero capillary pressure,
2 Base case; Brooks–Corey relation as explained in Table 3 with $\lambda = 2$,
3 High capillary pressure case representing a dense/tight rock; Brooks-Corey relation with $\lambda = 1$, and
4 A modification of capillary pressure to model the salt self-enhancing phenomenon; an average between the base case ($\lambda = 2$) and a high capillary pressure case with $\lambda = 0.5$ as described in the following.

We implemented the modification of capillary pressure to model the self-enhancing salt nucleation and precipitation mechanism described in Miri et al. (2015). To do so, the capillary pressure of the cells with solid was modified with a weighting factor to allow flow of water into the dried-out domain.

$$P_c = (1 - \beta)P_c^{base} + \beta P_c^{\max} \tag{41}$$

$$\beta = \frac{S_{salt}}{S_{salt}^{\max}},\ S_{salt}^{\max} = 0.8 \tag{42}$$

where P_c^{base} represent capillary pressure of the undamaged rock and

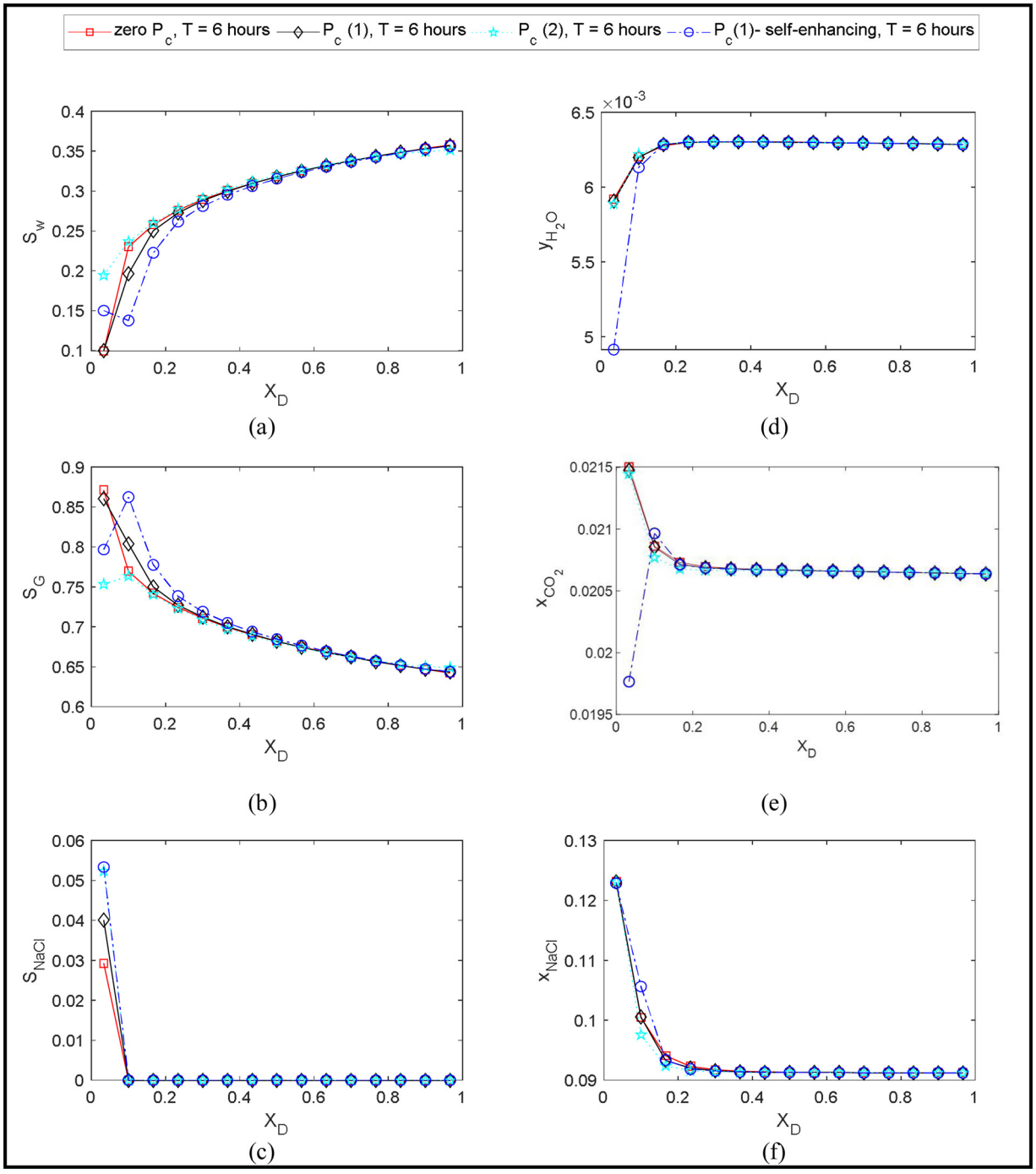

Fig. 14. Sensitivity analysis of capillary pressure on Water, CO_2 and salt saturation and concentration along the core at different time steps during displacement of brine by CO_2 (Base Case, Salinity = 25 wt%).

P_c^{max} represent capillary pressure of a rock which is completely filled by an aggregate of micro-meter size salt crystals. The weighting factor, β, allows for interpolation between these two extreme bounds. β is the fraction of the damaged porous media and *1- β* represents the undamaged zone where the salt aggregates formed. The P_c^{max} can be directly measured, but weighting factor, ultimately needs to be matched against experimental data. We have tested our proposed formulation assuming P_c^{max} follows Brooks-Corey relation with $\lambda = 0.5$.

In all of the tested cases, residual water saturation is 0.35, however, due to vaporization, water saturation reaches to values lower than residual water saturation until minimum water saturation, 0.1. Therefore, the capillary pressure is extended to below the residual saturation following same formulation (Fig. 13).

Figs. 14 and 15 present the results of the sensitivity analysis of capillary pressure. Results show that owing to the water mass exchange in the dry-out zone, a saturation gradient forms across the drying front (Fig. 14-a and b). This will, in turn, give rise to a capillary pressure gradient which drives the water toward the evaporation front, supporting more evaporation. In addition, as the water is evaporated more into the CO2 stream, salt concentration in the trapped brine increases, resulting in more salt deposition (Fig. 14-c). Our results confirm that activating the capillary pressure option in the simulations only alters the precipitation patterns and has a limited effect on the amount of precipitation, as it is confirmed by Pruess and Müller (2009). In

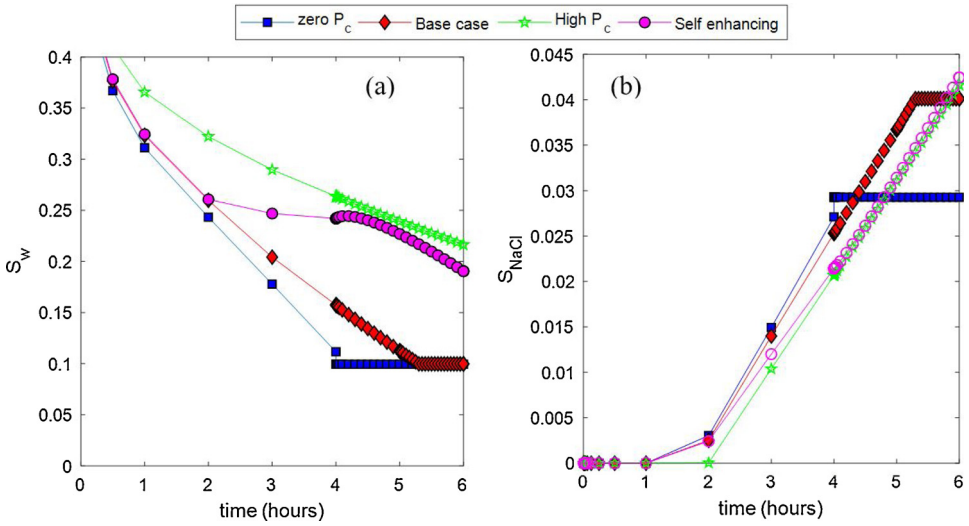

Fig. 15. Sensitivity analysis of capillary pressure on water and solid (NaCl) phase in the first grid at different times.

addition, for a same injection flow rate, the higher the capillary pressure the more the salt precipitates behind the evaporation front (Fig. 14-c). Hurter et al. (2007) pointed out that capillarity is a significant driver to the salt formation so that no precipitation will occur if one disregard it in the simulations. However, our simulation with zero capillary pressure shows that salt deposition will happen even if this option is not activated (Fig. 14-c). Moreover, it turned out that activating the self-enhancing option would create an additional saturation gradient across the drying front (significant capillarity owing to microporous structure of salt aggregates) and drives the water toward the evaporation front, supporting more evaporation (Figs. 14-a and 15 -a). This type of capillary pressure, however, is not similar (in terms of its origin) to the rock capillary pressure. In the self-enhancing process, the salt aggregates growing in the gas phase provide further surface area for evaporation (Fig. 14-b). This behaviour is mimicked by the weighting factor, β, which varies over time. Fig. 15-a has shown that owing to strong capillary suction of precipitated salt, the extent of precipitation could be much greater than the salt content in the residual trapped water alone (Figs. 14-c and 15 -b).

4.6. Injection flow rate

CO_2 injection flow rate has a determinative role in the injectivity calculation. The competence between the capillary force and convective force will determine the impact of injection flow rate. A sensitivity analysis on injection flow rate has been performed and results are presented in Fig. 16. Our simulations showed that the extent of salt precipitation is determined by vaporization rate which mostly is controlled by the injection rate. The results show that at higher injection flow rate, rate of water evaporation also increases and therefore evaporation front progresses with a higher velocity, leaving a homogenous salt deposition behind in the dried zone. A lower injection rate, however, will induce a higher capillary back flow towards the evaporation surface, thus suppressing the effect of pressure gradient. The enhanced capillary flow, in turn, increases the possibility of intensive salt accumulation close to the inlet.

4.7. Temperature

The maximum solubility limit of halite in brine solution and also the phase behaviour of CO_2-Brine system are mainly driven by temperature. As it is shown in Fig. 3, increasing temperature noticeably raises solubility of water in the CO_2 phase, enhancing rate of evaporation. As a result, the water quickly reaches its saturation limit and salt will precipitate. A sensitivity analysis on temperature has been performed and results are illustrated in Figs. 17 and 18 . As it is shown, temperature largely alters the distribution of salt, yet the extent of salt precipitation remains unchanged. The progress of drying front is also enhanced with increasing temperature.

5. Conclusions

In this study, we present a novel approach for incorporating formation drying-out and halite-precipitation modelling into compositional AD-MRST software. To do so, an accurate and reliable fluid model ePC-SAFT which can effectively account for ionic effects is developed and implemented into MRST compositional. The thermodynamic model is verified against binary mixture data and also a more complex asphaltenic fluid. It is shown that the fluid model can successfully model both evaporation and salting-out effect. To prove the validity of the simulator, we have benchmarked it against several well-known examples with analytical solutions demonstrating ability of the code covering a variety of physical mechanisms. Finally, to realize the capability of the new model to represent different physics of salt precipitation, we have simulated the injection of dry CO_2 into a brine saturated core-scale domain and performed sensitivity analyses over various parameters. The model can describe the amount of precipitation in an equilibrium or kinetic approach (i.e., depending on how far the salt saturation is from the solubility limit). Our results also show that for high reaction rate constants, both approaches give similar results. We also proposed a modification of capillary pressure to model the salt self-enhancing phenomenon. It is shown that under certain thermophysical conditions belonging to the capillary drying regime salt might massively precipitate during the course of CO_2 injection. We also show that the extent of evaporation and the induced formation damage is primarily controlled by the porosity-permeability relations. However, due to interplay of multiple counteractive parameters, assessment of the risk of formation damage need to be evaluated for each setting separately.

CRediT authorship contribution statement

S. Parvin: Software, Visualization, Writing - review & editing. **M. Masoudi:** Software, Validation, Writing - review & editing. **A. Sundal:** Funding acquisition, Project administration, Resources. **R. Miri:** Supervision, Conceptualization, Methodology, Writing - original draft, Writing - review & editing.

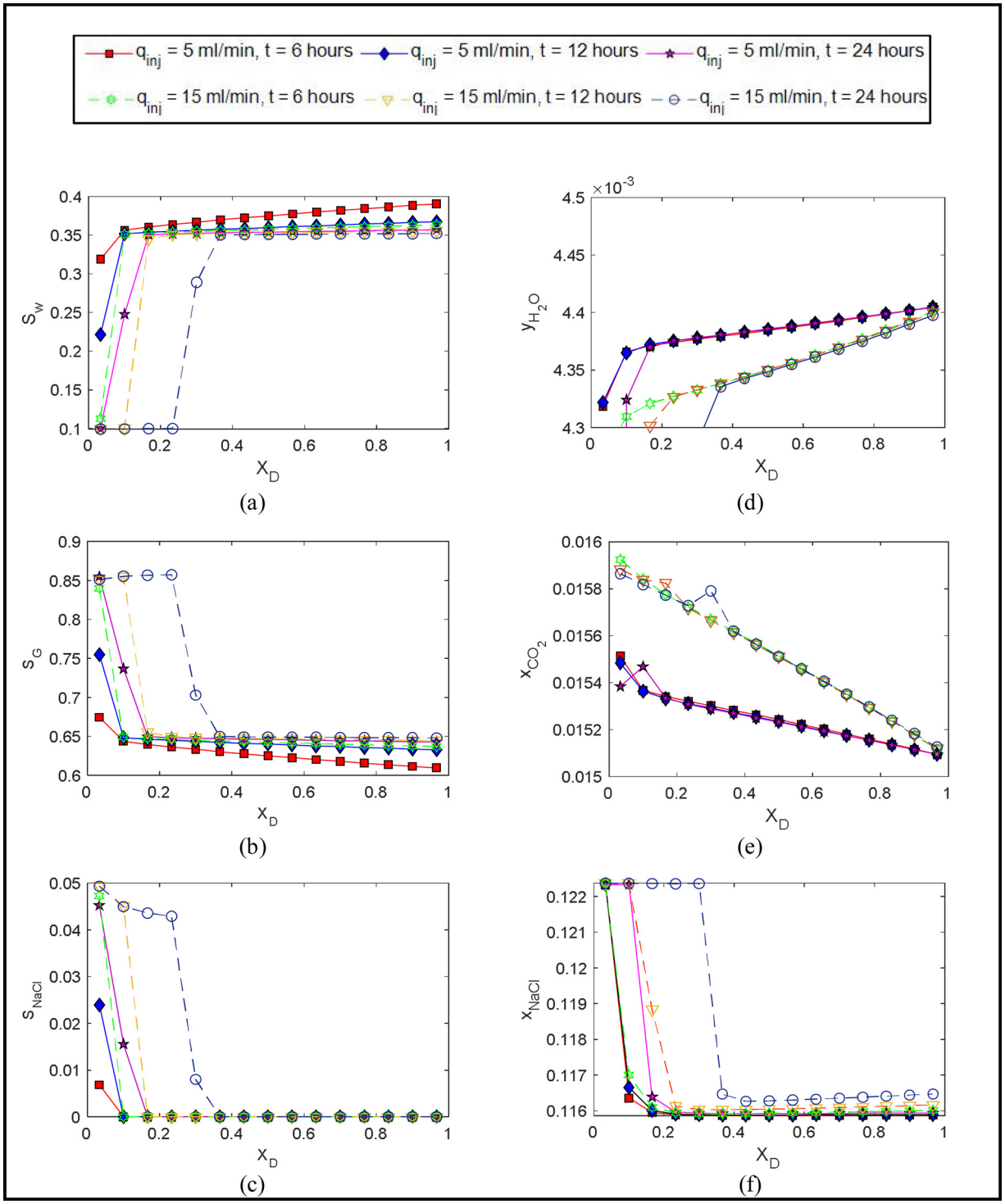

Fig. 16. Sensitivity analysis of injection rate on Water, CO_2 and salt saturation and concentration along the core at different time steps during displacement of brine by CO_2 (Base Case, Salinity = 25 wt%).

Declaration of Competing Interest

The authors declare that they have no known competing financial interests or personal relationships that could have appeared to influence the work reported in this paper.

Acknowledgements

A.S and R.M acknowledge the funding received for this work by the Research Council of Norway (RCN) and industry partners through the project CO_2 UPSLOPE. M.M acknowledges the funding received for this study from the POREPAC project “Preventing loss of near-well permeability in CO2 injection wells”, which is supported by the Research Council of Norway through the CLMIT program (280651/E20). We thank our colleagues from SINTEF Digital (Olav Møyner and Halvor M. Nilsen) who provided insight and expertise that greatly assisted the research.

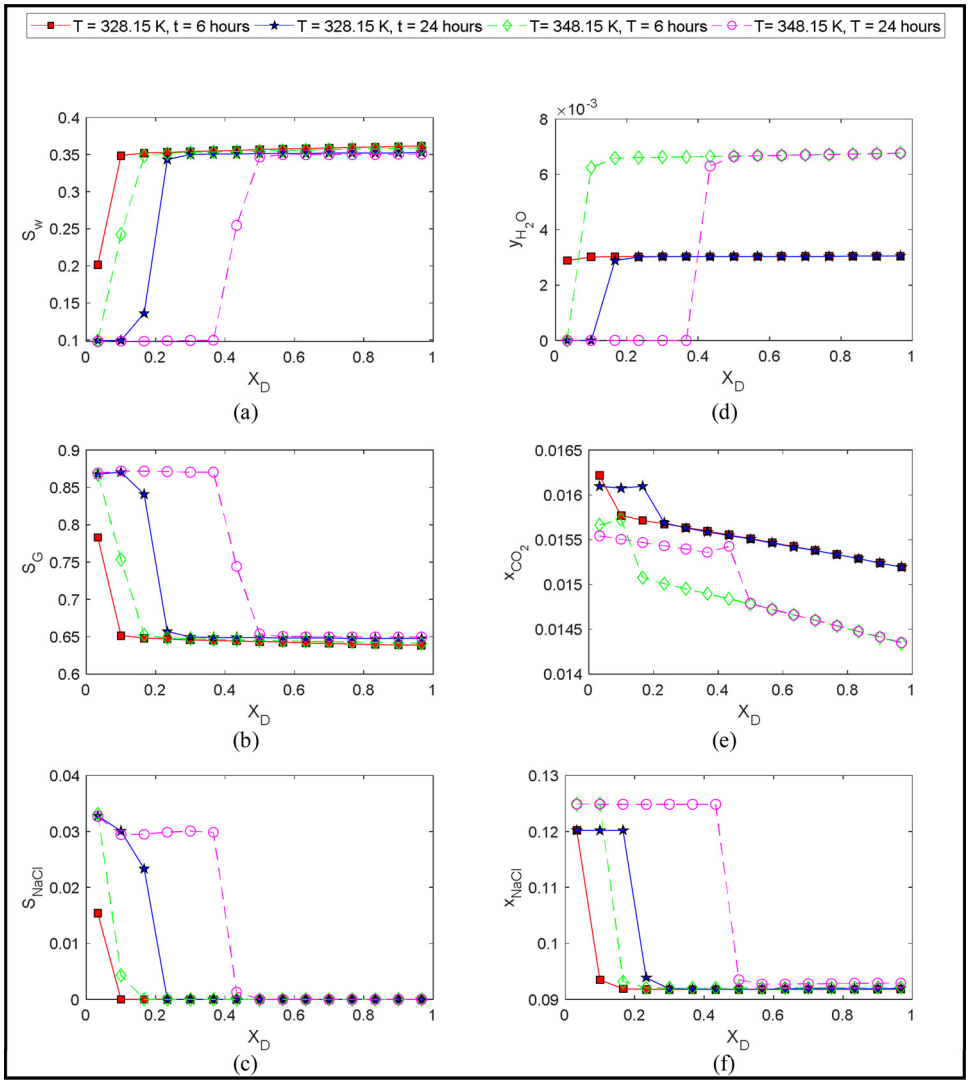

Fig. 17. Sensitivity analysis of temperature on Water, CO_2 and salt saturation and concentration along the core at different time steps during displacement of brine by CO_2 (Base Case, Salinity = 25 wt%).

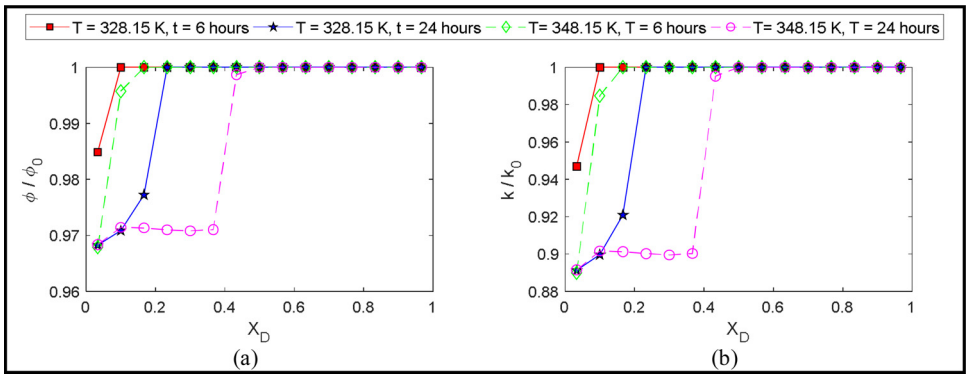

Fig. 18. Sensitivity analysis of temperature on temporal evolution of porosity and permeability along the core.

Appendix A. Supplementary data

Supplementary material related to this article can be found, in the online version, at doi:https://doi.org/10.1016/j.ijggc.2020.103075.

References

André, L., Peysson, Y., Azaroual, M., 2014. Well injectivity during CO_2 storage operations in deep saline aquifers – Part 2: Numerical simulations of drying, salt deposit mechanisms and role of capillary forces. Int. J. Greenh. Gas Control 22, 301–312. https://doi.org/10.1016/j.ijggc.2013.10.030.

Bacci, G., Korre, A., Durucan, S., 2011. Experimental investigation into salt precipitation during CO_2 injection in saline aquifers. Energy Procedia 4, 4450–4456. https://doi.org/10.1016/j.egypro.2011.02.399.

Bacci, G., Durucan, S., Korre, A., 2013. Experimental and numerical study of the effects of halite scaling on injectivity and seal performance during CO_2 injection in saline aquifers. Energy Procedia 37, 3275–3282. https://doi.org/10.1016/j.egypro.2013.06.215.

Bachu, S., Adams, J.J., 2003. Sequestration of CO_2 in geological media in response to climate change: capacity of deep saline aquifers to sequester CO_2 in solution. Energy Convers. Manage. 44, 3151–3175.

Bao, K., Lie, K.A., Møyner, O., Liu, M., 2017. Fully implicit simulation of polymer flooding with MRST. Comput. Geosci. https://doi.org/10.1007/s10596-017-9624-5.

Baumann, G., Henninges, J., De Lucia, M., 2014. Monitoring of saturation changes and salt precipitation during CO_2 injection using pulsed neutron-gamma logging at the Ketzin pilot site. Int. J. Greenh. Gas Control 28, 134–146. https://doi.org/10.1016/j.ijggc.2014.06.023.

Bette, S., Heinemann, R.F., 1989. Compositional modeling of high-temperature gas-condensate reservoirs with water vaporization. Proceedings of the Society of Petroleum Engineers of AIME, (Paper) SPE.

Buckley, S.E., Leverett, M.C., 1942. Mechanism of fluid displacement in Sands. Trans. AIME. https://doi.org/10.2118/942107-g.

Cameretti, L.F., Sadowski, G., Mollerup, J.M., 2005. Modeling of aqueous electrolyte solutions with perturbed-chain statistical associated fluid theory. Ind. Eng. Chem. Res. 44, 3355–3362. https://doi.org/10.1021/ie0488142.

Chapman, W.G., Gubbins, K.E., Jackson, G., Radosz, M., 1989. SAFT: equation-of-state solution model for associating fluids. Fluid Phase Equilib. 52, 31–38.

Chapman, W.G., Gubbins, K.E., Jackson, G., Radosz, M., 1990. New reference equation of state for associating liquids. Ind. Eng. Chem. Res. 29, 1709–1721.

Driesner, T., 2007. The system H_2O–NaCl. Part II: Correlations for molar volume, enthalpy, and isobaric heat capacity from 0 to 1000°C, 1 to 5000bar, and 0 to 1 XNaCl. Geochim. Cosmochim. Acta 71, 4902–4919. https://doi.org/10.1016/j.gca.2007.05.026.

Driesner, T., Heinrich, C.A., 2007. The system H_2O–NaCl. Part I: Correlation formulae for phase relations in temperature–pressure-composition space from 0 to 1000°C, 0 to 5000bar, and 0 to 1 XNaCl. Geochim. Cosmochim. Acta 71, 4880–4901. https://doi.org/10.1016/j.gca.2006.01.033.

Flemisch, B., Darcis, M., Erbertseder, K., Faigle, B., Lauser, A., Mosthaf, K., Müthing, S., Nuske, P., Tatomir, A., Wolff, M., 2011. DuMux: DUNE for multi-{phase, component, scale, physics,…} flow and transport in porous media. Adv. Water Resour. 34, 1102–1112.

Gross, J., Sadowski, G., 2001. Perturbed-chain SAFT: an equation of state based on a perturbation theory for chain molecules. Ind. Eng. Chem. Res. 40, 1244–1260. https://doi.org/10.1021/ie0003887.

Gross, J., Sadowski, G., 2002. Application of the perturbed-chain SAFT equation of state to associating systems. Ind. Eng. Chem. Res. 41, 5510–5515.

Grude, S., Landrø, M., Dvorkin, J., 2014. Pressure effects caused by CO_2 injection in the Tubåen Fm., the Snøhvit field. Int. J. Greenh. Gas Control 27, 178–187. https://doi.org/10.1016/J.IJGGC.2014.05.013.

Hassanzadeh, H., 2006. Mathematical Modeling of Convective Mixing in Porous Media for Geological CO_2 Storage.

Held, C., Reschke, T., Mohammad, S., Luza, A., Sadowski, G., 2014. ePC-SAFT revised. Chem. Eng. Res. Des. 92, 2884–2897. https://doi.org/10.1016/J.CHERD.2014.05.017.

Hommel, J., Coltman, E., Class, H., 2018. Porosity-permeability relations for evolving pore space: a review with a focus on (bio-)geochemically altered porous media. Transp. Porous Media 124, 589–629. https://doi.org/10.1007/s11242-018-1086-2.

Hurter, S., Labregere, D., Berge, J., 2007. Simulations for CO_2 injection projects with compositional simulator. Proceedings of the Offshore Europe Conference. https://doi.org/10.2523/108540-ms.

Ji, X., Held, C., Sadowski, G., 2012. Modeling imidazolium-based ionic liquids with ePC-SAFT. Fluid Phase Equilib. 335, 64–73. https://doi.org/10.1016/J.FLUID.2012.05.029.

Kim, M., Sell, A., Sinton, D., 2013. Aquifer-on-a-chip: understanding pore-scale salt precipitation dynamics during CO_2 sequestration. Lab Chip 13, 2508. https://doi.org/10.1039/c3lc00031a.

Kleinitz, W., Dietzsch, G., Köhler, M., 2003. Halite scale formation in gas-producing wells. Chem. Eng. Res. Des. 81, 352–358. https://doi.org/10.1205/02638760360596900.

Lie, K.A., Aarnes, J.E., Gimse, T., 2007. An introduction to the numerics of flow in porous media using matlab. Geometric Modell. Numer. Simul. Optim. Appl. Math. SINTEF. https://doi.org/10.1007/978-3-540-68783-2_9.

Masoudi, M., Miri, R., Hellevang, H., Kord, S., 2020. Modified PC-SAFT characterization technique for modeling asphaltenic crude oil phase behavior. Fluid Phase Equilib. 513, 112545. https://doi.org/10.1016/j.fluid.2020.112545.

Maxwell, D., Keith, K., 2014. Concept, design and implementation of a halite scale mitigation completion in a gas well. Proceedings of the Society of Petroleum Engineers - SPE International Conference and Exhibition on Oilfield Scale 2014.

McWhorter, D.B., Sunada, D.K., 1990. Exact integral solutions for two-phase flow. Water Resour. Res. https://doi.org/10.1029/WR026i003p00399.

Michelsen, M.L., 1982. The isothermal flash problem. Part I. Stability. Fluid Phase Equilib. 9, 1–19. https://doi.org/10.1016/0378-3812(82)85001-2.

Miri, R., Hellevang, H., 2016. Salt precipitation during CO_2 storage–a review. Int. J. Greenh. Gas Control. https://doi.org/10.1016/j.ijggc.2016.05.015.

Miri, R., Aagaard, P., Hellevang, H., 2014. Examination of CO_2–SO_2 solubility in water by SAFT1. Implications for CO_2 transport and storage. J. Phys. Chem. B 118, 10214–10223. https://doi.org/10.1021/jp505562j.

Miri, R., van Noort, R., Aagaard, P., Hellevang, H., 2015. New insights on the physics of salt precipitation during injection of CO_2 into saline aquifers. Int. J. Greenh. Gas Control 43, 10–21. https://doi.org/10.1016/j.ijggc.2015.10.004.

Mohamed, I., Nasr-El-Din, H.A., 2013. Fluid/Rock Interactions During CO2 Sequestration in Deep Saline Carbonate Aquifers: Laboratory and Modeling Studies. SPE J. 18, 468–485. https://doi.org/10.2118/151142-PA.

Mohebbinia, S., 2013. Advanced Equation of State Modeling for Compositional Simulation of Gas Floods. The University of Texas at Austin.

Nghiem, L.X., Li, Y.-K., 1984. Computation of multiphase equilibrium phenomena with an equation of state. Fluid Phase Equilib. 17, 77–95. https://doi.org/10.1016/0378-3812(84)80013-8.

Nooraiepour, M., Fazeli, H., Miri, R., Hellevang, H., 2018. Effect of CO_2 phase states and flow rate on salt precipitation in shale caprocks - a microfluidic study. Environ. Sci. Technol. https://doi.org/10.1021/acs.est.8b00251.

Ott, H., de Kloe, K., Marcelis, F., Makurat, A., 2011. Injection of supercritical CO_2 in brine saturated sandstone: pattern formation during salt precipitation. Energy Procedia 4, 4425–4432. https://doi.org/10.1016/J.EGYPRO.2011.02.396.

Ott, H., de Kloe, K., van Bakel, M., Vos, F., van Pelt, A., Legerstee, P., Bauer, A., Eide, K., van der Linden, A., Berg, S., Makurat, A., 2012. Core-flood experiment for transport of reactive fluids in rocks. Rev. Sci. Instrum. 83, 084501. https://doi.org/10.1063/1.4746997.

Ott, H., Snippe, J., de Kloe, K., Husain, H., Abri, A., 2013. Salt precipitation due to Sc-gas injection: single versus multi-porosity rocks. Energy Procedia 37, 3319–3330. https://doi.org/10.1016/j.egypro.2013.06.220.

Wang, Y., Luce, T., Ishizawa, C., Shuck, M., Smith, K., Ott, H., Appel, M., 2010. Halite precipitation and permeability assessment during supercritical CO2 core flood. International Symposium of the Society of Core Analysis. Halifax, pp. 4–7.

Peaceman, D.W., 1983. Interpretation of well-block pressures in numerical reservoir simulation with nonsquare grid blocks and anisotropic permeability. Soc. Pet. Eng. J. 23, 531–543.

Peysson, Y., 2012. Permeability alteration induced by drying of brines in porous media. Eur. Phys. J. Appl. Phys. 60, 24206. https://doi.org/10.1051/epjap/2012120088.

Privat, R., Gani, R., Jaubert, J.-N., 2010. Are safe results obtained when the PC-SAFT equation of state is applied to ordinary pure chemicals? Fluid Phase Equilib. 295, 76–92. https://doi.org/10.1016/j.fluid.2010.03.041.

Pruess, K., 1991. TOUGH2-A General-purpose Numerical Simulator for Multiphase Fluid and Heat Flow.

Pruess, K., Müller, N., 2009. Formation dry-out from CO_2 injection into saline aquifers: 1. Effects of solids precipitation and their mitigation. Water Resour. Res. 45. https://doi.org/10.1029/2008WR007101.

Rachford Jr, H.H., Rice, J.D., 1952. Procedure for use of electronic digital computers in calculating flash vaporization hydrocarbon equilibrium. J. Pet. Technol. Altern. Fuels 4, 13–19.

Roels, S.M., Ott, H., Zitha, P.L.J., 2014. μ-CT analysis and numerical simulation of drying effects of CO_2 injection into brine-saturated porous media. Int. J. Greenh. Gas Control 27, 146–154.

Spycher, N., Pruess, K., Ennis-King, J., 2003. CO_2-H_2O mixtures in the geological sequestration of CO_2. I. Assessment and calculation of mutual solubilities from 12 to 100°C and up to 600 bar. Geochim. Cosmochim. Acta 67, 3015–3031. https://doi.org/10.1016/S0016-7037(03)00273-4.

Tan, S.P., Adidharma, H., Radosz, M., 2005. Statistical associating fluid theory coupled with restricted primitive model to represent aqueous strong electrolytes. Ind. Eng. Chem. Res. 44, 4442–4452. https://doi.org/10.1021/ie048750v.

Verma, A., Pruess, K., 1988. Thermohydrological conditions and silica redistribution near high-level nuclear wastes emplaced in saturated geological formations. J. Geophys. Res. https://doi.org/10.1029/JB093iB02p01159.

Wang, Y., Liu, Y., 2013. Impact of capillary pressure on permeability impairment during CO_2 injection into deep saline aquifers. J. Cent. South Univ. 20, 2293–2298. https://doi.org/10.1007/s11771-013-1736-z.

Yan, W., Huang, S., Stenby, E.H., 2011. Measurement and modeling of CO_2 solubility in NaCl brine and CO_2–saturated NaCl brine density. Int. J. Greenh. Gas Control 5, 1460–1477. https://doi.org/10.1016/j.ijggc.2011.08.004.

Zeidouni, M., Pooladi-Darvish, M., Keith, D., 2009. Analytical solution to evaluate salt precipitation during CO2 injection in saline aquifers. Int. J. Greenh. Gas Control 3, 600–611. https://doi.org/10.1016/J.IJGGC.2009.04.004.

Zhang, Y., Isaj, E., 2015. Halite envelope for downhole salt deposition prediction and management. Proceedings of the SPE - European Formation Damage Conference, EFDC.